Uncertainties in the attenuation performance of a multi-frequency metastructure from additive manufacturing

Adriano T. Fabro[a,*], Han Meng[b] and Dimitrios Chronopoulos[b]

[a]Department of Mechanical Engineering, University of Brasilia, 70910-900, Brasilia, Brazil
[b]Institute for Aerospace Technology & The Composites Group, University of Nottingham, NG8 1BB, Nottingham, UK

Abstract

Additive manufacturing has been used to propose several designs of phononic crystals and metamaterials due to the low cost to produce complex geometrical features. However, like any other manufacturing process, it can introduce material and geometrical variability in the nominal design and therefore affect the structural dynamic performance. Locally resonant metamaterials are typically designed such that the distributed resonators have the same natural frequency or, in the case of rainbow metastructures, a well-defined spatial profile. In this work, the effects of the break of periodicity caused by additive manufacturing variability on the attenuation performance of a multi-frequency metastructure is investigated. First, an experimental investigation on the manufacturing tolerances of test samples produced from a Selective Laser Sintering process are assessed and variability levels are used to propose a random field model for the metastructure. Subsequently, the stochastic model is used to investigate the vibration suppression performance of broadband multi-frequency metastructures. An analytical model based on a transfer matrix approach is used to calculate transfer receptance due to a point time harmonic force in a finite length metastructure, which is composed of evenly spaced non-symmetric resonators attached to a beam with Π-shaped cross-section. This design creates a multi-frequency metastructure, i.e. band gaps in more than one frequency band. Individual samples of the random fields are used to show that the mistuned resonators can change the vibration attenuation performance of the metastructure and that even small levels of variability, given by less than 1% for the masse and less than 3% for the Young's modulus can have a significant effect on the overall vibration attenuation performance of the metastructure when considered together. It is also shown that different spatial profiles can have a significant effect on the vibration attenuation performance in both band gaps. Therefore, the modelling of the uncertainty metastructures has to take into account the spatial correlation of the properties of the metastructure resonators. The obtained results are expected to be useful for further robust design in mass produced industrial applications.

Keywords: vibration attenuation, rainbow metamaterial, additive manufacturing, uncertainties

1. Introduction

Additive manufacturing (AM) has been used to propose several designs of phononic crystals and metamaterials due to the low cost to produce complex geometrical features and has the potential to make them feasible in several industrial applications [1] along with the use of smart structures (e.g. [2]). However, like any other manufacturing process, AM can introduce material and geometrical variability in the nominal design [3,4] and therefore affect the structural dynamic performance. Currently, there is few experimental work available in the literature investigating metamaterial performance for vibration attenuation applications (e.g. [5–10]) and most of them do not consider the effects of spatially correlated disorder on the band gap.

*Corresponding author
Email address: fabro@unb.br (A.T. Fabro)

The use of resonators for vibration control has been successfully used for decades in engineering applications [11]. Interestingly, it can be shown that the actual working mechanism for vibration attenuation of metamaterials is related to the vibration absorber principle [12], known as Mie-type or Fabry-Perot-type resonances [13]. Although, the efficacy of a single resonator is typically restricted to very narrow frequency bands, with several developments in the last decades to widen it (e.g. [14]), the powerful concept introduced by locally resonant metamaterial is that is possible to significantly widen the attenuation band simply by adding more resonators while not necessarily increasing the mass ratio. Moreover, some of the well-established concepts from smart structures can also be applied to metastructures [2,15,16] for further improvement on its vibration attenuation performance. Metastructures can be particularly useful and has been recently explored in lightweight Noise, Vibration and Harshness (NVH) applications [17–19], for instance. Further widening on the attenuation band can also be achieved by multi-resonant metamaterials. In this context, mass-in-mass lattices have been proposed to in acoustic [20] and structural metamaterials [21]. Also, a similar effect can be achieved by using a two or multiple degree-of-freedom array of resonators [20–25] instead of a single resonator design. Multi-resonators design have also been explored in more complex structures with encouraging results for industrial applications [9,10].

It has been shown that the break of periodicity introduced by the spatial variability of material and geometrical properties of metastructures creates a resonator mistuning which can induce wave trapping and thus greatly affecting the vibration attenuation performance by either band gap annihilation or attenuation bandwidth widening, depending on the imposed spatial profile [6]. Overall, there is a need to investigate the effects of the manufacturing variability on the performance of metastructures [1,26–29], which can also affect the coupling of the metastructures to the vibration source and receiver [30]. Near-periodic structures are referred herein as systems where material or geometric properties vary spatially following a deterministic function or a random field.

In this work, the effects of the break of periodicity caused by additive manufacturing variability on the attenuation performance of a multi-frequency metastructure is investigated. Section 2 presents an analytical model for a metastructure with two non-symmetric resonators, evenly spaced and attached to a beam with Π -shaped cross-section. Section 0 presents an investigation of the manufacturing variability introduced by the available 3D printed. A random field model is proposed based on the experimental results to represent the effects of the resonators mistuning and near-periodicity. In Section 4, numerical results are presented for some highlighted individual samples numerically generated from the proposed random field model and also from a second random field model, considering only randomness on the resonators tip masses. First, the effects of individual samples of the metastructures are analysed and the main physical consequences of the break in the periodicity are discussed. Then, the response statistics are analysed using Monte Carlo sampling as a stochastic solver. Finally, Section 5 presents some concluding remarks.

2. Metamaterial beam with non-symmetric resonators

In this section, the proposed metastructure and an analytical model for beam with two non-symmetric resonators, shown in Figure 1, is briefly presented, such that the frequency response function can be efficiently predicted. The metastructure is composed of a total of 17 unit cells with two non-symmetric cantilever-mass attached and acting like local resonators. In the proposed design, each resonator can act independently such that it is possible to create two separate band gap regions, thus broadening the total attenuation band.

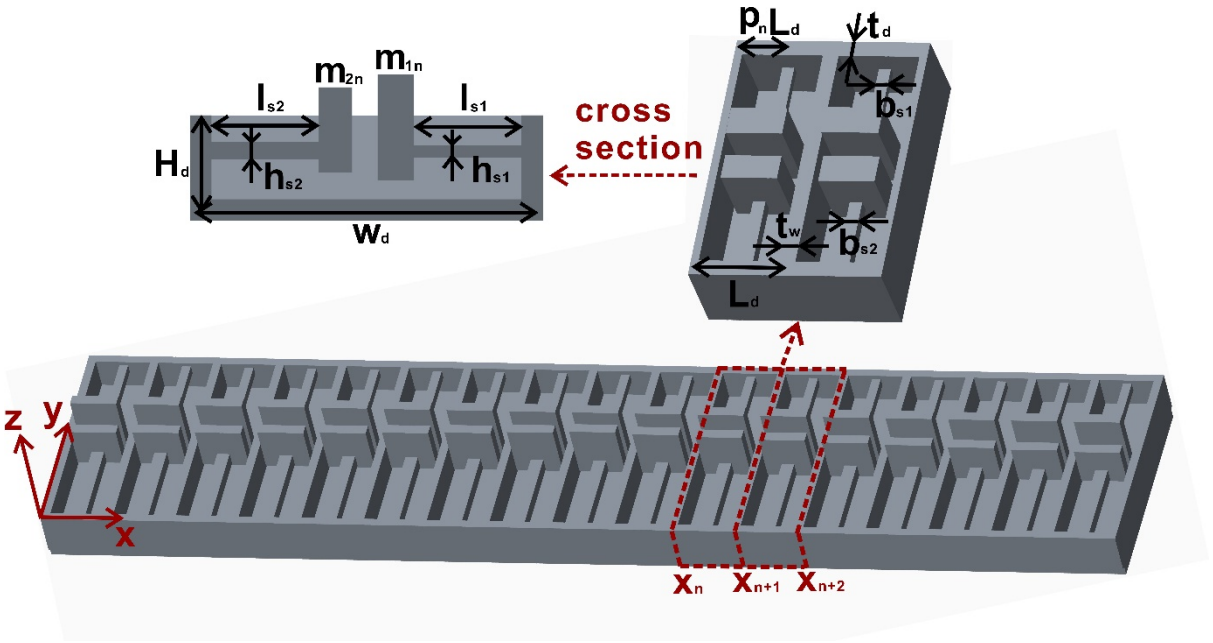

Figure 1: Schematic representations of the metamaterial beam at each unit cell and a diagram of the unit cell of Π-shaped beam with non-symmetric resonators.

2.1. Free wave propagation

It is assumed a Euler-Bernoulli beam theory for both the baseline host structure and the cantilever-mass resonator. Each resonator is modelled as a beam point attached to the baseline structure at one end and a lumped mass with negligible inertia at the other. Displacements of the n-th and $(n+1)$-th segments of the Π-shaped beam as shown in Figure 1, can be written as

$$\begin{aligned}
W_{n,l} &= \alpha_{n,l}e^{-ik(x-x_n)} + \beta_{n,l}e^{-k(x-x_n)} + \chi_{n,r}e^{ik(x-x_n)} + \varepsilon_{n,r}e^{k(x-x_n)},\\
W_{n,r} &= \alpha_{n,r}e^{-ik\left(x-(x_n+p_nL_d)\right)} + \beta_{n,r}e^{-k\left(x-(x_n+p_nL_d)\right)} + \chi_{n,r}e^{ik\left(x-(x_n+p_nL_d)\right)} + \\
&\qquad \varepsilon_{n,r}e^{k\left(x-(x_n+p_nL_d)\right)},\\
W_{n+1,l} &= \alpha_{n+1,l}e^{-ik(x-x_{n+1})} + \beta_{n+1,l}e^{-k(x-x_{n+1})} + \chi_{n+1,l}e^{ik(x-x_{n+1})} + \varepsilon_{n+1,l}e^{k(x-x_{n+1})},\\
W_{n+1,r} &= \alpha_{n+1,r}e^{-ik\left(x-(x_{n+1}+p_{n+1}L_d)\right)} + \beta_{n+1,r}e^{-k\left(x-(x_{n+1}+p_{n+1}L_d)\right)}\\
&\qquad + \chi_{n+1,r}e^{ik\left(x-(x_{n+1}+p_{n+1}L_d)\right)} + \varepsilon_{n+1,r}e^{k\left(x-(x_{n+1}+p_{n+1}L_d)\right)},
\end{aligned} \tag{1}$$

where $W_{i,l}$ and $W_{i,l}$, $i = 1,2,\ldots$ are the displacements before and after the resonators of the i-th segment, respectively, x_i is the position of the i-th plate insertion in x direction, $k = (\rho A/EI_z)^{1/4}\sqrt{\omega}$, A and I_z are the cross section area and moment of inertia of the Π-shaped beam, ρ is the density of the rainbow metamaterial, L_d is the distance between periodic plate insertions, p_iL_d represents the position of the resonators inside the i-th segment of the metamaterial beam.

The resonators are modelled as point attachments displacements at the n-th segment, where continuity of displacement, slope and equilibrium of bending moment and shearing force inside the segment are given as

$$
\begin{aligned}
W_{n,l}\big|_{x=x_n+p_nL_d} &= W_{n,r}\big|_{x=x_n+p_nL_d},\\
W_{n,l}^{'}\big|_{x=x_n+p_nL_d} &= W_{n,r}^{'}\big|_{x=x_n+p_nL_d},\\
W_{n,l}^{''}\big|_{x=x_n+p_nL_d} &= W_{n,r}^{''}\big|_{x=x_n+p_nL_d},\\
EI_zW_{n,l}^{'''}\big|_{x=x_n+p_nL_d} + F_n &= EI_zW_{n,r}^{'''}\big|_{x=x_n+p_nL_d},
\end{aligned}
\tag{2}
$$

where F_n is the interaction force between the two resonators and the Π-shaped beam inside the n-th segment. From these relations, the displacement fields presented in Eq. (1) can be rewritten in a matrix form for the wave propagation in a single segment, or unit cell, such that

$$
\mathbf{R}_n\mathbf{\Lambda}_{n,l}\left[\alpha_{n,l},\beta_{n,l},\chi_{n,l},\varepsilon_{n,l}\right]^T = \mathbf{R}_{\mathrm{c}}\left[\alpha_{n,r},\beta_{n,r},\chi_{n,r},\varepsilon_{n,r}\right]^T \tag{3}
$$

where

$$
\mathbf{R}_c = \begin{bmatrix} 1 & 1 & 1 & 1 \\ -i & -1 & i & 1 \\ -1 & 1 & -1 & 1 \\ iEI_zk^3 & -EI_zk^3 & -iEI_zk^3 & EI_zk^3 \end{bmatrix}, \tag{4}
$$

is due to displacement, rotation, shearing force and bending moment at the right end while

$$
\mathbf{R}_n = \begin{bmatrix} 1 & 1 & 1 & 1 \\ -i & -1 & i & 1 \\ -1 & 1 & -1 & 1 \\ \left(iEI_zk^3 + N_{s,n}\right) & \left(-EI_zk^3 + N_{s,n}\right) & \left(-iEI_zk^3 + N_{s,n}\right) & \left(iEI_zk^3 + N_{s,n}\right) \end{bmatrix}, \tag{5}
$$

is given at the left end, where $N_{s,n}$ is the force exerted on the Π-shaped beam by both resonators. A more detailed derivation of this interaction is given in further a paper from the authors. Moreover, $\mathbf{\Lambda}_{n,l} = \mathrm{diag}[\exp(-ip_{n+1}L_d), \exp(-p_{n+1}L_d), \exp(ip_{n+1}L_d), \exp(p_{n+1}L_d)]$ is the propagation matrix, where diag[·] stands for diagonal matrix, which relates the wave amplitudes at both left and right ends.

Additionally, the periodic plate insertions are modelled as added masses to the Π-shaped beam at the ends of each segment. Thus, considering the continuities of displacement, slope and equilibrium conditions of the plate insertions, the displacement relationship between the n-th and $(n+1)$-th segments can be written as

$$
\begin{aligned}
W_{n,r}\big|_{x=x_{n+1}} &= W_{n+1,l}\big|_{x=x_n+1},\\
W_{n,r}^{'}\big|_{x=x_n+1} &= W_{n+1,l}^{'}\big|_{x=x_n+1},\\
EI_zW_{n,r}^{''}\big|_{x=x_{n+1}} - J_f\omega^2W_{n,r}^{'}\big|_{x=x_n+1} &= EI_zW_{n+1,l}^{''}\big|_{x=x_{n+1}},\\
EI_zW_{n,r}^{'''}\big|_{x=x_n+1} + m_f\omega^2W_{n,r}\big|_{x=x_{n+1}} &= EI_zW_{n,l}^{'''}\big|_{x=x_n+1},
\end{aligned}
\tag{6}
$$

where m_f and J_f are the mass and moment of inertia of the plate insertions. From these relations, the displacement fields presented in Eq. (1) can be rewritten in a matrix and the wave amplitudes are related by

$$
\mathbf{R}\left[\alpha_{n+1,l},\beta_{n+1,l},\chi_{n+1,l},\varepsilon_{n+1,l}\right]^T = \mathbf{U}\mathbf{\Lambda}_{n,r}\left[\alpha_{n,r},\beta_{n,r},\chi_{n,r},\varepsilon_{n,r}\right]^T, \tag{7}
$$

where

$$\mathbf{R} = \begin{bmatrix} 1 & 1 & 1 & 1 \\ -i & -1 & i & 1 \\ -EI_z k^2 & EI_z k^2 & -EI_z k^2 & EI_z k^2 \\ iEI_z k^3 & -EI_z k^3 & -iEI_z k^3 & iEI_z k^3 \end{bmatrix}, \tag{8}$$

$$\mathbf{U} = \begin{bmatrix} 1 & 1 & 1 & 1 \\ -i & -1 & i & 1 \\ -\left(iEI_z k^2 + iJ_f \omega^2 k\right) & \left(iEI_z k^2 + iJ_f \omega^2 k\right) & -\left(iEI_z k^2 + iJ_f \omega^2 k\right) & \left(iEI_z k^2 + iJ_f \omega^2 k\right) \\ \left(iEI_z k^3 + m_f \omega^2\right) & \left(-EI_z k^3 + m_f \omega^2\right) & \left(-iEI_z k^3 + m_f \omega^2\right) & \left(iEI_z k^3 + m_f \omega^2\right) \end{bmatrix}, \tag{9}$$

express the continuity and equilibrium conditions and the wave propagation is given by the matrix $\mathbf{\Lambda}_{n,l} = \text{diag}[\exp(-ik(1-p_n)L_d), \exp(-k(1-p_n)L_d), \exp(ik(1-p_n)L_d), \exp(k(1-p_n)L_d)]$. The obtained wave amplitudes from the continuity and equilibrium conditions at the resonators point attachments, Eq. (3) and added plate insertions, Eq. (7) are then combined to obtain a the displacement transfer matrix between the n-th and the $(n+1)$-th segment, i.e.

$$\left[\alpha_{n+1,l}, \beta_{n+1,l}, \chi_{n+1,l}, \varepsilon_{n+1,l}\right]^T = \mathbf{T}_n \left[\alpha_{n,l}, \beta_{n,l}, \chi_{n,l}, \varepsilon_{n,l}\right]^T, \tag{10}$$

where $\mathbf{T}_n = \mathbf{R}^{-1}\mathbf{U}\mathbf{\Lambda}_{n,r}\mathbf{R}_c^{-1}\mathbf{R}_n\mathbf{\Lambda}_{n,l}$. Subsequently, the transfer matrix approach can be used to relate the first to the $(n+1)$-th segment as

$$\left[\alpha_{n+1,l}, \beta_{n+1,l}, \chi_{n+1,l}, \varepsilon_{n+1,l}\right]^T = \mathbf{\Xi} \left[\alpha_{1,l}, \beta_{1,l}, \chi_{1,l}, \varepsilon_{1,l}\right]^T, \tag{11}$$

where $\mathbf{\Xi} = \mathbf{T}_n\mathbf{T}_{n-1}\ldots\mathbf{T}_1$. For a periodic structure, the transfer matrix $\mathbf{T}_n$ is identical for every segment. Consequently, according to the Bloch theorem [31,32], a wavenumber k_n can be defined from the propagation constant $\mu_n = \exp(-ik_n L_d)$, which is given from the transfer matrix of the periodic metamaterial such that

$$|\mathbf{T}_n - \mu_n \mathbf{I}| = 0. \tag{12}$$

However, this assumption does not hold when variability effects are taken into account thus breaking the periodicity of the metastructure. In this sense, an equivalent wavenumber k_T is also defined from the propagation constant $\mu_T = \exp(-ik_T L)$ of the finite length metamaterial with spatially varying properties, i.e. near-periodic, as

$$|\mathbf{\Xi} - \mu_T \mathbf{I}| = 0, \tag{13}$$

The equivalent wavenumber k_T can be also interpreted as the wavenumber when the finite rainbow metamaterial is a periodic unit of an infinite complex beam and it represents the total phase change and attenuation of a travelling wave over m unit cells. It is used as a tool to understand the wave-like behaviour of non-periodic structures. Note that the total phase and attenuation change $k_T L$, which is a

complex number for the case of metastructure, is not generally equal to the contribution of the phase and attenuation change at each segment in the near periodic metastructure, i.e., $k_T L \neq \sum_{n=1}^{m} k_n L_d$. This is because of the additional scattering created due to the differences in neighbouring segments. However, it can be shown that $k_T L \approx \sum_{n=1}^{m} k_n L_d$ for the case of slowly varying properties in which this internal scattering is negligible [33].

2.2. Forced response of a finite length metastructure

The forced response is given assuming a finite length near-periodic metastructure excited at one end by a point harmonic force of amplitude F. Equilibrium of force and momentum at both ends, $x = 0$ and $x = L$, of the rainbow metamaterial are given as

$$\begin{aligned} F + m_f\omega^2\, W_{1,l}\big|_{x=0} &= EI_z W_{1,l}^{'''}\big|_{x=0}, \\ -J_f\omega^2 W_{1,l}^{'}\big|_{x=0} &= EI_z W_{1,l}^{''}\big|_{x=0}, \\ EI_z W_{q,r}^{''}\big|_{x=L} + m_f\omega^2 W_{m,r}\big|_{x=L} &= 0, \\ EI_z W_{m,r}^{'''}\big|_{x=L} + J_f\omega^2 W_{m,r}^{'}\big|_{x=L} &= 0, \end{aligned} \tag{14}$$

where m is the number of segments of the ∏-shaped beam, $L = mL_d$ is the length of the metastructure. According to Eq. (7), Eq. (11) and Eq. (14), the displacement at the right end $x = L$ of the metamaterial beam can be expressed as

$$W_{m,r}\big|_{x=L} = \alpha_{m,r} e^{-ik(1-p_s)L_d} + \beta_{m,r} e^{-k(1-p_s)L_d} + \chi_{m,r} e^{ik(1-p_s)L_d} + \varepsilon_{m,r} e^{k(1-p_s)L_d} \tag{15}$$

where $\left[\alpha_{m,r}, \beta_{m,r}, \chi_{m,r}, \varepsilon_{m,r}\right]^T = \mathbf{\Pi\Psi}^{-1}\,[0, F, 0, 0]^T$, with $\mathbf{\Pi} = \mathbf{R_c^{-1}} \mathbf{R}_{\mathrm{m}} \mathbf{\Lambda_{m,l}} \mathbf{T}_{\mathrm{m-1}} \mathbf{T}_{\mathrm{m-2}} \ldots \mathbf{T_1}$, and a 4×4 matrix $\mathbf{\Psi} = [\mathbf{\Psi}_1 \quad \mathbf{\Psi}_2\,]^T$, in which

$$\mathbf{\Psi_1} = \begin{bmatrix} \left(-EI_z k^2 + ikJ_f\omega^2\right) & \left(EI_z k^2 - kJ_f\omega^2\right) & \left(-EI_z k^2 + ikJ_f\omega^2\right) & \left(EI_z k^2 + kJ_f\omega^2\right) \\ \left(iEI_z k^3 + m_f\omega^2\right) & \left(-EI_z k^3 - m_f\omega^2\right) & \left(-iEI_z k^3 - m_f\omega^2\right) & \left(EI_z k^3 + m_f\omega^2\right) \end{bmatrix}, \tag{16}$$

and

$$\mathbf{\Psi_2} = \begin{bmatrix} \left(-EI_z k^2 + ikJ_f\omega^2\right) & \left(EI_z k^2 + kJ_f\omega^2\right) & \left(-EI_z k^2 - ikJ_f\omega^2\right) & \left(EI_z k^2 - kJ_f\omega^2\right) \\ \left(iEI_z k^3 + m_f\omega^2\right) & \left(-EI_z k^3 + m_f\omega^2\right) & \left(-iEI_z k^3 + m_f\omega^2\right) & \left(EI_z k^3 + m_f\omega^2\right) \end{bmatrix} \mathbf{\Lambda}_{q,r} \mathbf{\Pi}. \tag{17}$$

Finally, the receptance function of the metastructure, i.e. the displacement per unit force, is then given by

$$R_{ec} = 20 \log_{10} \left| \frac{W_{m,r}\big|_{x=L}}{F} \right|. \tag{18}$$

A similar expression can be found for the receptance at others positions inside the metastructure.

3. Manufacturing variability on the periodic design

Recently, research effort is being directed to uncertainty quantification and stochastic modelling (UQSM) of mechanical, geometrical and dimensional properties of structures produced from additive manufacturing [34–36]. Typically, trial-and-error is employed to get high quality products, which

constitutes a major hurdle for this kind of manufacturing process [37]. Several processing considerations have to be taken in to account, like heat distribution, laser parameters and so on [4,38,39] For comprehensive UQSM on structural dynamics applications, focus should be given in macro or meso scale mechanical parameters rather than on variability from process parameters [40]. In this sense, Machado et al. [41] estimated spatially correlated variability of the Young's modulus, modelled a Gaussian random field, using a model updating approach. Beli et al. [6] has proposed a random field identification approach based on sides blocks printed along the metastructure and has shown that this kind of uncertainty can play a major role on the performance of locally resonating metastructures. Both works have shown that some analytical model of spatial correlation function can accurately represent the spatial uncertainty of polyamide beams produced by Selective Laser Sintering (SLS).

In this section, the material and geometrical variability introduced by the additive manufacturing process in the nominal design is discussed. An experimental investigation is carried out with a total of 15 test samples produced by SLS. The test samples are beams with prismatic cross-section with 10 mm × 4 mm × 80 mm. The mass and dimensions of each sample were measured by a precision scale and a digital caliper, while the Young's modulus was measured by a universal test machine, shown in Figure 2. The obatined mean value, standard deviation and coefficient of variation COV, i.e., the standard deviation over mean value, are presented in Table 1 for the mass density and Young's modulus. The measured dimensions of the test samples presented negligible variability, which shows that the SLS is much more accurate for geometric than for material properties. This result is similar to the obtained by Beli et al. [6]. The considered metastructure is 490 mm length with 17 unit cells, therefore the test samples are approximately 2.5 larger than the unity cell. It means that the Young's modulus and mass density spatial variability of the test sample is averaged out more significantly than for the unit cell, thus reducing the overall dispersion. This effect is similar to the local average process as described by Vanmarke [42], which does not affect the mean value but can reduce the estimated variance.

Table 1: The mean value, standard deviation and coefficient of variation COV of the Young's modulus, density and mass of the 15 test samples.

	E, MPa	ρ, kg/m^3	m, g
Mean	1621.7	948.9	3.16
Standard deviation	49.9	7.4	0.03
COV, %	3.07	0.78	0.95

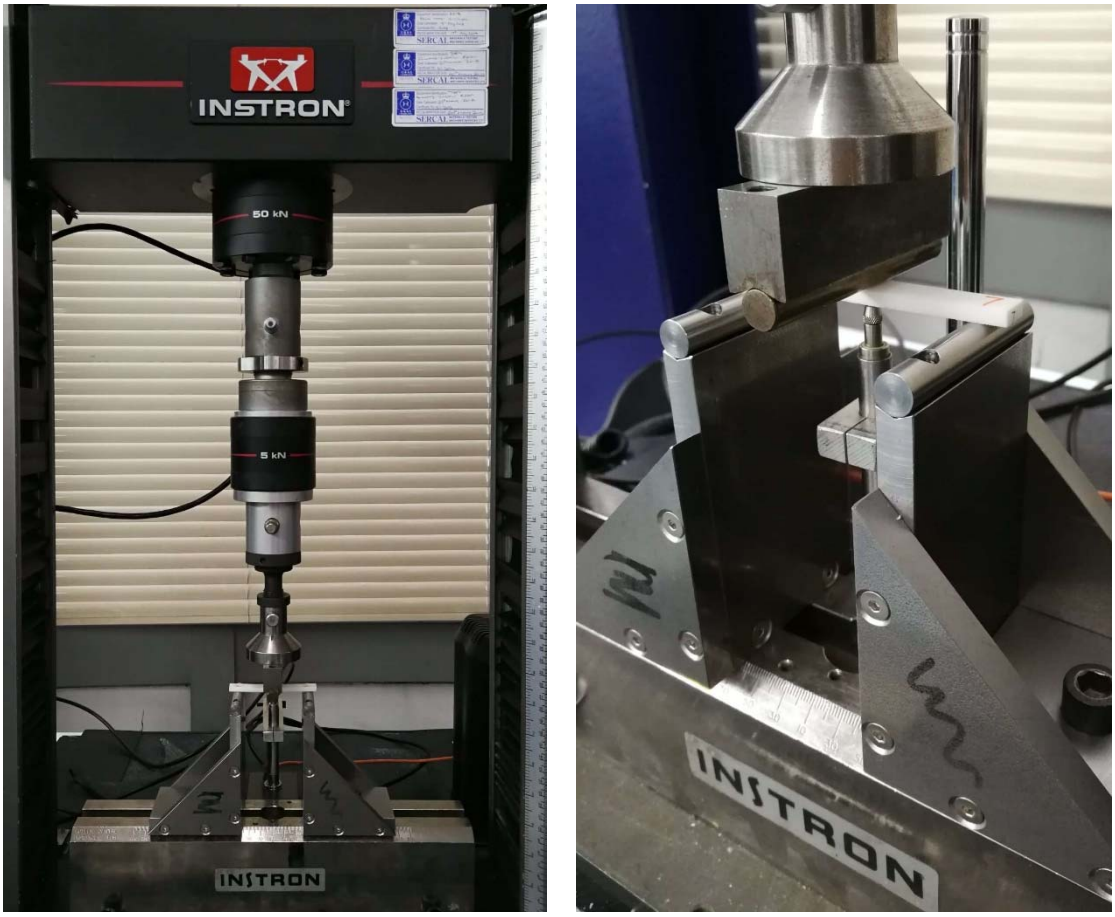

(a) (b)

Figure 2: (a) Universal test machine with test sample produced by Selective Laser Sintering and (b) detailed visualization of the test setup.

Figure 3 presents the scatter plot of the mass density and Young's modulus of the 15 test samples. It can be clearly noticed that both Young's modulus and mass are correlated, most likely due to the porosity of the samples. Although the obtained results are very specific to the printer and the printing process used to manufacture the metastructure, the analytical model presented in the previous section requires the characterization of a few parameters, such as the Young's modulus and mass density. Typically, this information be made available from the printer's manufacturer or other reliable source. In addition to the dispersion and correlation between the Young's modulus and mass density, a random field model has to be introduced to properly represent the mistuning of the resonators in the metastructure, i.e., the spatial changes also introduced by manufacturing variability.

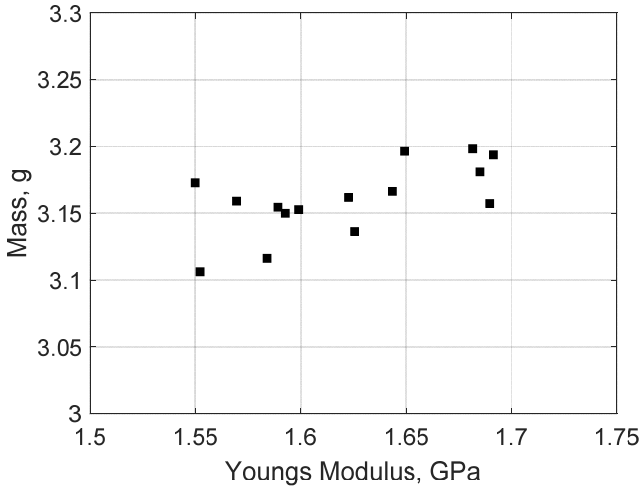

Figure 3: Scatter plot of the mass and Young's modulus of the 15 test samples.

3.1. Resonators mistuning and near-periodicity

One of the most important effects for the vibration attenuation performance is the mistuning of the resonators [5,6], which is caused by the spatial profile on the material properties created due to the manufacturing variability. In this section, the effects of the mistuning of resonators are modelled. It is assumed that the material variability can be represented by a change on the resonators mass, given by a lumped parameter in the analytical model, and by the Young's modulus, assumed constant within each unity cell.

To include the random spatial variability on the analytical model, a random field model is assumed based on available experimental results in 3D printed structures [6]. Random fields are multidimensional random processes and can be used to model spatially distributed variability using a probability measure [42]. The random field is Gaussian if its random variables are Gaussian and it can be completely defined by its mean value, standard deviation and correlation function $C(\tau)$, where τ is the lag, i.e. the distance between any two points in the homogeneous random field. The manufacturing variability is assumed to be given by a Gaussian Homogeneous random field $H_1(x)$ for each mass, i.e. the both masses at each unity cell have the same statistical properties, and $H_2(x)$ for the Young's modulus, both with same correlation function $C(\tau) = \exp(-\tau/c_l)$, where c_l is the correlation length, i.e., the level of statistical fluctuation of the spatial variability. In other words, this parameter controls the smoothness of the spatial variation, given the spatial profile of the tip masses of the resonators along the beam.

Due to the discrete nature of the resonators tip mass, the random fields $H_{1,2}(x)$ are discretized over the metamaterial length such that it is approximated by the random vector $\boldsymbol{\xi}_{\mathrm{m}}$. The discretization process also results in a correlation matrix $\mathbf{C}$ from $C(\tau)$ [43]. Similarly, the Young's modulus that is assumed constant within each unit cell can be represented by a random vector $\boldsymbol{\xi}_{\mathrm{E}}$. This approach is known as the midpoint method, first introduced by Der Kiureguian [44] for random field discretization. Moreover, results shown in Figure 3 suggests that both random fields are correlated, with correlation coefficient $\rho_{E,m} = 0.6359$.

Let $\boldsymbol{\zeta}$ be a vector of uncorrelated Gaussian random zero mean and unit variance variables and with $\mathbf{C} = \langle \boldsymbol{\xi}\boldsymbol{\xi}^T \rangle$ the correlation matrix, where $\langle \cdot \rangle$ represents the mathematical expectation and T stands for transpose. This matrix is symmetric and positive-definite, so it is possible to apply a Cholesky decomposition of the kind $\mathbf{C} = \boldsymbol{\Sigma}\boldsymbol{\Sigma}^{\mathrm{T}}$, where $\boldsymbol{\Sigma}$ is a lower triangular matrix. A realization of the random

field can be given by $\boldsymbol{\xi} = \boldsymbol{\Sigma}\,\boldsymbol{\zeta}$ [45], and the both tip masses and Young's modulus at each unit cell are respectively given by

$$\mathbf{m}_{1,2} = m_{0_{1,2}}(\mathbf{1} + \sigma_m \boldsymbol{\xi}_{\mathrm{m}}), \qquad \mathbf{E} = E_0(\mathbf{1} + \sigma_E \boldsymbol{\xi}_{\mathrm{E}}), \tag{19}$$

where $m_{0_{1,2}}$ and E_0 are the nominal values of the resonators tip masses and Young's modulus in the periodic design, $\mathbf{1}$ is a vector $m \times 1$ vector filled with 1 and $\sigma_{E,m}$ controls the level of statistical dispersion of the random vector. From this expression, both random fields are subsequently correlated using the estimated correlation coefficient $\rho_{E,m}$.

4. Numerical results

In this section, a numerical analysis is carried out considering the mean value of density and Young's modulus given in Table 1, Poisson ratio $\nu = 0.3$ and structural damping $\eta = 0.02$. Each cantilever beam or resonator, named 1 and 2, presented height $h_{s1} = 1.4$ mm, $h_{s2} = 2.3$ mm, width $b_{s1} = 1.9$ mm, $b_{s2} = 2.3$ mm and length $l_{s1} = l_{s2} = 21.2$ mm, as described in Figure 1. The baseline or host beam presents a Π-shaped cross-section with height $H_d = 10$ mm and width $w_d = 51$ mm, side wall thickness $t_d = 2$ mm, bottom plate thickness $b_d = 5$ mm and lateral plate thickness $t_w = 2$ mm distanced by $L_d = 15$ mm, with a total of 17 unit cells and total beam length $L_T = 257$ mm. The tip mass in both resonators at each unit cell is assumed to have a mean value of 1 g. Note that, in this case, the difference in length of the beams produces the differences in the resonance frequencies and therefore in the band gaps.

Figure 4(a) presents the amplitude of the transfer receptance of proposed metastructure considering the nominal periodic design from 0 Hz to 350 Hz at steps of 0.5 Hz and Figure 4(b) presents the real and imaginary parts of the normalized equivalent wavenumber from a unit cell, as described in Eq. (12). Note that $|\mathrm{Re}\{k_n L_d/\pi\}| \leq 1$ due to the periodic nature of the metastructure, where L_d is the length of periodic unit cell. For a lossless waveguide, real wavenumber indicates purely propagating waves, imaginary wavenumber indicates evanescent waves while complex wavenumber indicates oscillating and decaying waves. From Figure 4(a), it can be seen that each resonator acts independently and creates a respective locally resonant band gap, significantly improving the vibration attenuation at more than one frequency band. This is also seen by the complex nature of the equivalent wavenumber at the band gaps in Figure 4(b), indicating highly attenuating effects. Note that at the attenuation band, the vibration amplitude reaches – 128 dB, which effectively stands for almost no vibration. Bragg-scattering type of band gaps are not created in this case because of the level of structural damping η of the metastructure, which is high enough to have the effect of annihilating them [46]. On the other hand, the added damping has the effect of broadening the band gap created due to the resonators but reducing amplitude of the attenuation [47]. It can also be noted that the produced stop band effect was created at very low frequency acting at the lowest modes of the structure. From the dispersion curve it can be seen that the group velocity $c_g = \partial\omega/\partial k$ is zero at the resonators frequency and it is negative at the band gap, meaning that the velocity of energy transport is in the negative direction. Although it can be interpreted as a negative-going wave, an equivalent positive going wave mode is present, ensuring the energy transport also in positive direction [48]. This effect has been misunderstood as causing the vibration attenuation rather than the presence of complex wavenumbers. Moreover, the attenuation performance of the band gaps can be given in terms of both the frequency band in which the attenuation occurs and in terms of the maximum attenuation at a specific frequency. This can be clearly seen when comparing both band gaps.

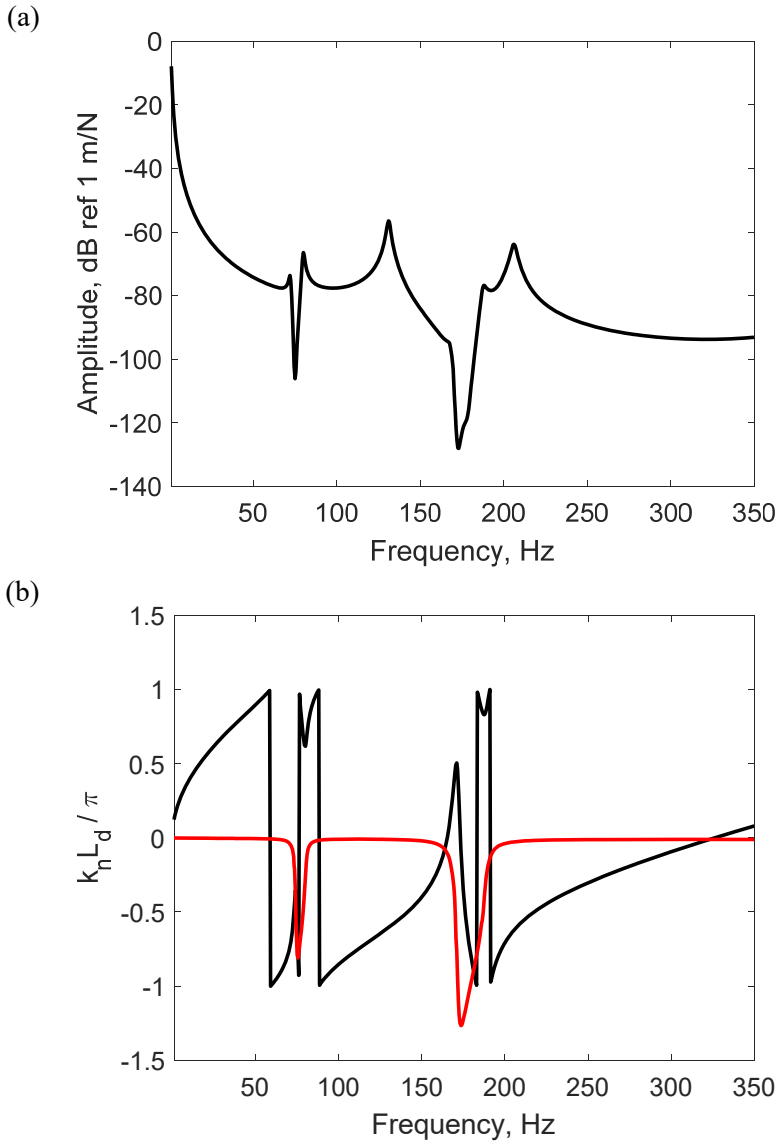

Figure 4**:** (a) Amplitude of the transfer receptance of proposed metastructure considering the nominal periodic design and (b) real (black) and imaginary (red) parts of the normalized equivalent wavenumber.

4.1. Effects of the manufacturing variability

In this section, the effects of manufacturing uncertainty are considered on the tip mass of both resonators and on the Young's modulus of the metastructure, represented by $\mathbf{m}_1$, $\mathbf{m}_2$ and $\mathbf{E}$ as described in section 3.1. It is considered that the tip masses of both resonators at each unit cell are identical, which is equivalent to assume that $\mathbf{m}_1 = \mathbf{m}_2$, and the dispersion parameters $\sigma_m = 0.01$ and $\sigma_E = 0.03$ are assumed to be the same as presented by the COV values shown in Table 1. Note that these are very low COV values. Additionally, a correlation length is assumed $c_l = 0.25L$, which is similar to the correlation length found in samples produced from additive manufacturing available in the literature [6,41]. First, the effects of individual samples of the metastructures are analysed and the main physical consequences of the break in the periodicity are discussed. Then, the ensemble statistics are presented and results are discussed. Monte Carlo sampling is used as the stochastic solver with the number of samples necessary for adequate stochastic convergence.

Figure 5 presents the spatial profile of the Young's modulus of the metastructure and the tip masses of the resonators. Note that the Young's modulus and tip masses distribution over the metastructure are

similar for both random samples due to the imposed correlation $\rho_{E,m}$ between these parameters, as described in Section 3.1. Figure 6(a) presents the amplitude of the transfer receptance of the metastructure for two random samples from which two cases are presented in yellow and red and have the corresponding tip masses and Young's modulus spatial profile shown as well. It can be seen that the vibration amplitude also reaches very low levels at the second band gap, with effectively almost no vibration, similar to the periodic case. Figure 6(b) shows the corresponding imaginary part of the normalized equivalent wavenumber. The real part is omitted such that the attenuation effects of the imaginary part of the wavenumber can be highlighted. Overall, it can be noticed that the mistuned resonators changed the vibration attenuation performance of the metastructure. The two highlighted cases present a qualitative difference in terms of band gap widening and maximum attenuation. The yellow case presents a smoother spatial profile when compared to the red case, even though they present a very similar statistical dispersion and have been generated from the same random field family. The smoother spatial profile created band gaps with larger maximum attenuation in both band gaps, while the rougher spatial profile had a decreased maximum attenuation performance but a wider band gap. This can be confirmed by the imaginary part of the corresponding wavenumber shown in Figure 6(b).
Finally, the mean value and 5th and 95th percentiles of the amplitude of the transfer receptance and the real and imaginary parts of the wavenumber of the metastructure is shown in Figure 7(a) and (b), respectively. Results are obtained with 1.000 Monte Carlo samples. Note that the 5th and 95th percentiles of the amplitude of the transfer receptance, Figure 7(a), show that vibration attenuation is likely to occur between 40 Hz and 200 Hz, where the spiky lower bound curve is given by the band gap shifting for the random samples. This result also show that the host structural behaviour is also affected, thus increasing the percentiles bounds for frequencies higher than the band gap. Note that the mean value (dashed line) is smoothed over the whole frequency range and therefore is not representative of the band gap performance. A similar behaviour is found on the real and imaginary parts of the wavenumber of the metastructure, Figure 7(b), i.e., a spiky upper and lower percentile bounds for both real and imaginary parts of the wavenumber, due to the band gap variability. For frequencies higher than the band gap, all of the variability on the receptance response can be attributed only to the real part of the wavenumber, which is related to the chances on the total mass and Young's modulus of the host structure.
It is remarkable that a coefficient of variability of less than 1% for $\mathbf{m}_1$ and $\mathbf{m}_2$ of 3% for $\mathbf{E}$ causes a very wide percentile interval along the frequency band containing the band gaps. Monte Carlo sampling considering only $\mathbf{m}_1$ and $\mathbf{m}_2$ or only $\mathbf{E}$ and not shown here, presented significantly smaller variability on the response. This is also confirmed by results further presented in Figure 7 of the next subsection, in which only $\mathbf{m}_1$ and $\mathbf{m}_2$ are considered to be random and the results do not present the same level of uncertainty even assuming a coefficient of variation of 10%. This result shown that even uncertain parameters with small levels of uncertainty can play an important role when combined with other parameters. In the next section, the effects of variability on the tip masses only is explored and discussed.

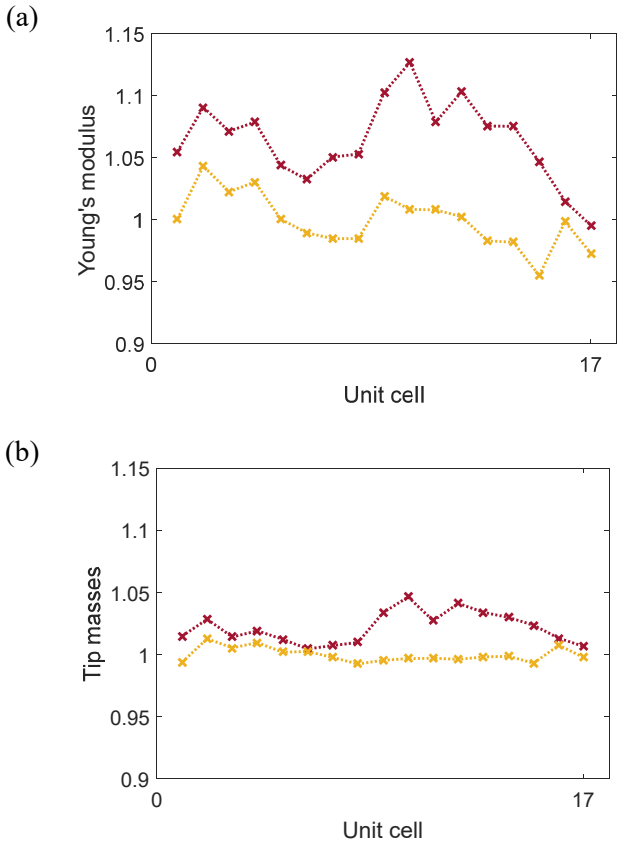

Figure 5: Two highlighted cases (yellow and red) of (a) the Young's modulus $\mathbf{E}$ and (b) the tip masses $\mathbf{m}_1$ and $\mathbf{m}_2$ spatial profile, considering $\mathbf{m}_1 = \mathbf{m}_2$ and correlated to $\mathbf{E}$ by $\rho_{E,m}$. Both cases are normalized by the nominal values E_0 and m_0, respectively.

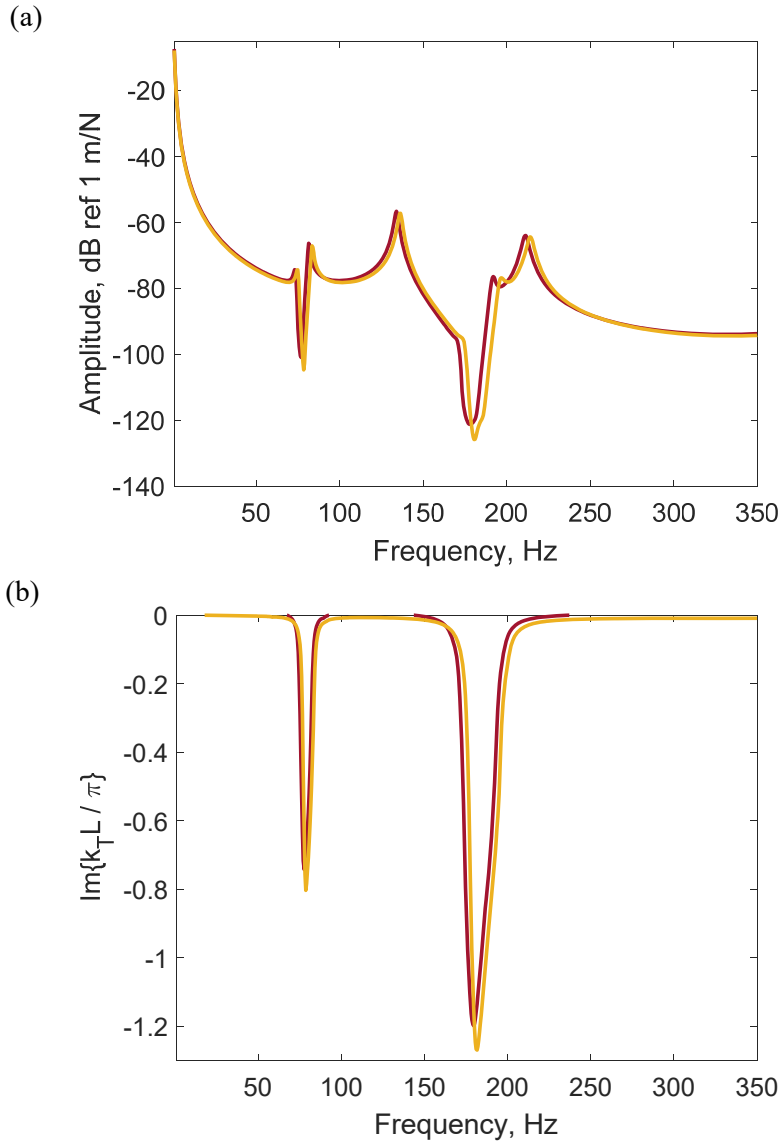

Figure 6: (a) Amplitude of the transfer receptance of the metastructure for two highlighted cases (yellow and red) from the random samples and (b) the corresponding imaginary part of the normalized equivalent wavenumber considering $\mathbf{m_1} = \mathbf{m_2}$ e correlated to $\mathbf{E}$ by $\rho_{E,m}$.

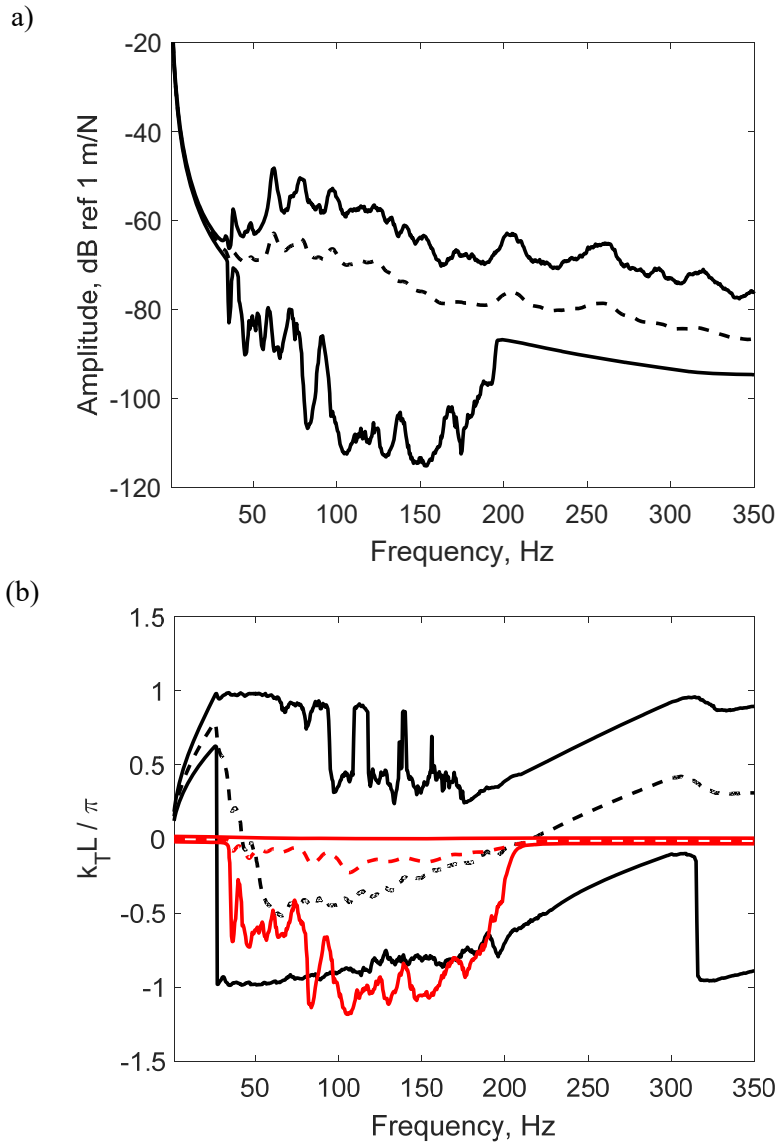

Figure 7: (a) The mean value (dashed line) and 5th and 95th percentiles (full line) of (a) the amplitude of the transfer receptance and (b) the real (black) and imaginary (red) parts of the metastructure considering $\mathbf{m}_1 = \mathbf{m}_2$ and correlated to $\mathbf{E}$ with the manufacturing variability.

4.2. Effects of uncertainty in the periodic design: random tip masses

In this section, the effects of manufacturing variability are considered only on the tip masses of the resonators assuming $\mathbf{m}_1$ and $\mathbf{m}_2$ have the similar statistical properties as presented in the previous sections but are independent. It means that changes in $\mathbf{m}_1$ can only affect the lowest band gap while changes in $\mathbf{m}_2$ can only affect the highest band gap.

Figure 8 shows the tip mass profile for $\mathbf{m}_1$ and $\mathbf{m}_2$ assuming the same correlation length, i.e. the same scale of spatial fluctuation, but with different levels of dispersion $\sigma_m = 0.15$, $\sigma_m = 0.10$, $\sigma_m = 0.05$, and $\sigma_m = 0.01$. Note that, although they are generated with the same statistical properties, i.e. with the same random field parameters, distinct spatial features can be seen on both cases, with a smoother profile for $\mathbf{m}_1$ when compared to $\mathbf{m}_2$. Figure 9(a) presents the amplitude of the transfer receptance of the metastructure for each case and Figure 9(b) shows the corresponding imaginary part of the normalized equivalent wavenumber.

(a)

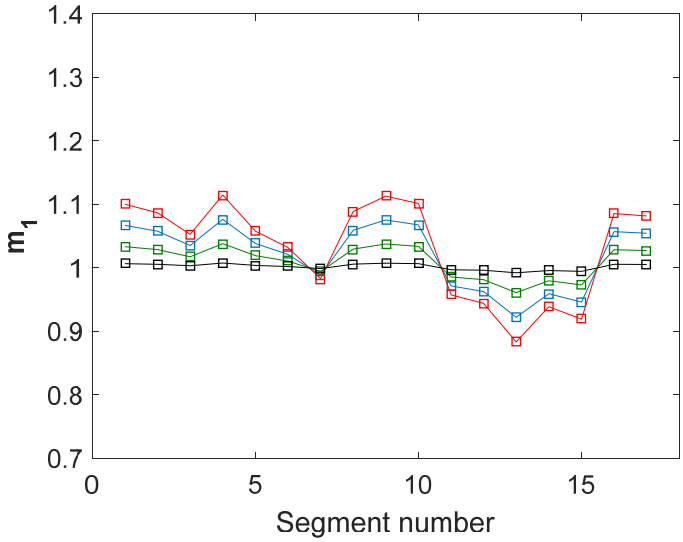

(b)

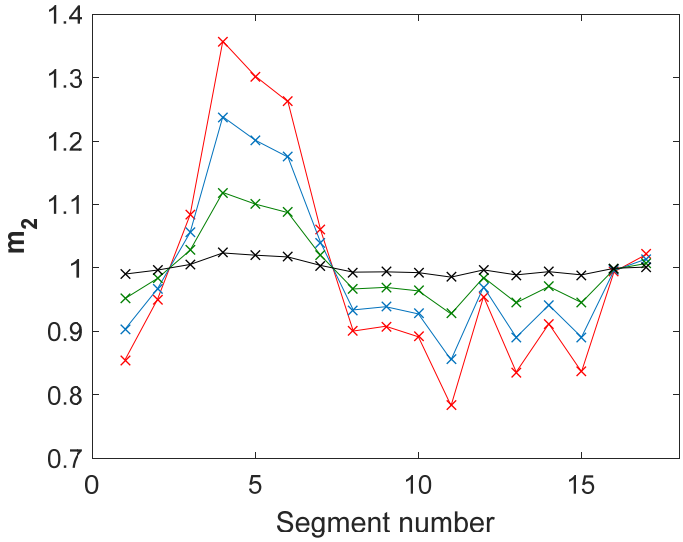

Figure 8**:** Highlighted case of independent realizations of the tip masses (a) $\mathbf{m}_1$ and (b) $\mathbf{m}_2$ assuming the same correlation length c_l and with dispersion $\sigma_m = 0.15$ (red line), $\sigma_m = 0.10$ (blue line), $\sigma_m = 0.05$, (green line) and $\sigma_m = 0.01$ (black line). Both masses are normalized by the nominal values m_0.

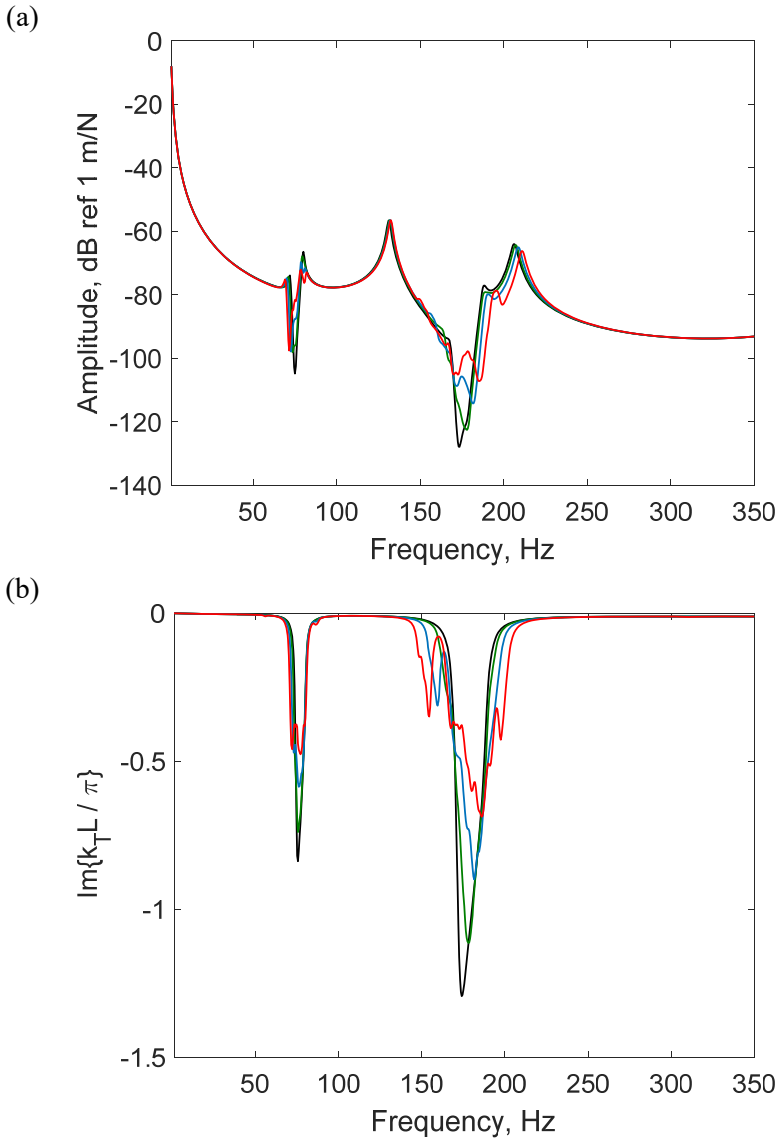

Figure 9**:** (a) Amplitude of the transfer receptance of the metastructure for the highlighted case and (b) the corresponding imaginary part of the normalized equivalent wavenumber. Independent realizations of $\mathbf{m}_1$ (dashed line with cross marker) and $\mathbf{m}_2$ (full line with square marker) are considered with the same correlation length c_l and with dispersion $\sigma_m = 0.15$ (red line), $\sigma_m = 0.10$ (blue line), $\sigma_m = 0.05$, (green line) and $\sigma_m = 0.01$ (black line).

A similar behaviour to the previous case can be observed in terms of the smoother and rougher spatial profile changing band gap widening and maximum attenuation, however in this case each band gap is affected in an independent manner due to the independence of $\mathbf{m}_1$ and $\mathbf{m}_2$. However, the highest band gap has a larger widening when compared to the lowest for increasing σ_m, as shown in Table 2.

Table 2: Band gap widening due to increasing dispersion σ_m of the tip mass profiles $\mathbf{m}_1$ and $\mathbf{m}_2$.

	$\Delta\omega_1/\omega_{01}$	$\Delta\omega_2/\omega_{02}$
$\sigma_m = 0.15$	0.21	0.37
$\sigma_m = 0.10$	0.20	0.32
$\sigma_m = 0.05$	0.19	0.27
$\sigma_m = 0.01$	0.18	0.26
periodic	0.18	0.26

Note that for $\mathbf{m}_2$, masses from unity cell 8 to 17 vary smoothly but present a rapid change from cells 1 to 7, while for $\mathbf{m}_1$ the masses vary smoothly from cell 1 to 17, overall. This difference caused qualitative changes on the band gaps created for each corresponding mass. Figure 10 presents the amplitude of the receptance along the metastructure for increasing dispersion values. Point harmonic excitation is given at position $x = 0$. The response at position $x = L$ is equivalent to the results shown in Figure 9(a). Note that for low dispersion levels, the band gap is created along the metastructure similarly to the periodic case, i.e. after a certain number of cells, no further widening is achieved [5]. However, for increasing σ_m, some increased vibration level is seen at the regions which were previously attenuated. This is created due to a transition from propagating to non-propagating waves, and vice-versa, along the metastructure at the same frequency. This transition is caused by differences of the locally defined wavenumber caused by the rapid $\mathbf{m}_2$ variation. Such transition causes wave reflection and it is known as a critical section sections [49] or as a turning point [50]. This transition can cause a significant wave reflection even though the metastructure properties vary slowly [49]. The spatial profile promotes a mistuning around the designed fundamental frequency of the resonators therefore creating an effect similar to a rainbow metamaterial [7,51,52].

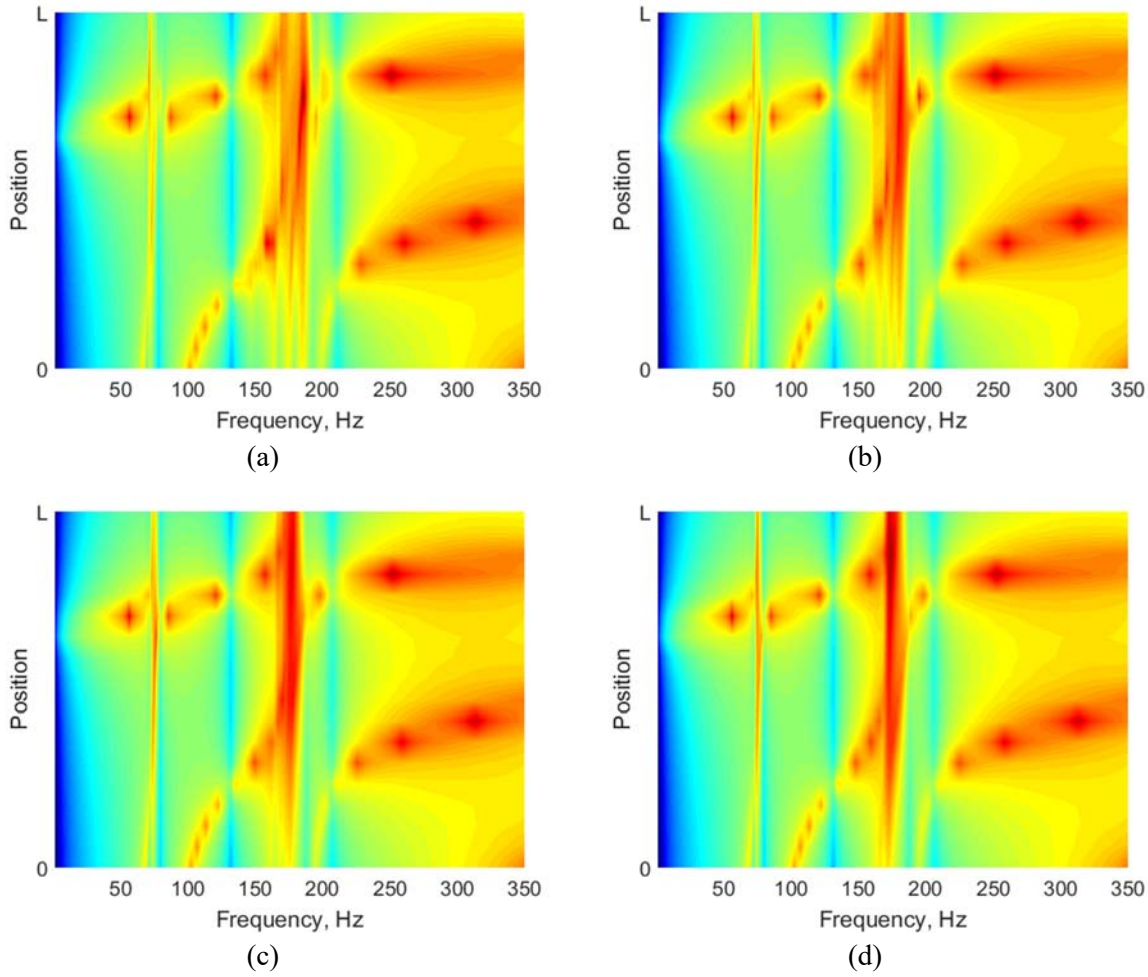

Figure 10**:** Amplitude of the receptance along the metastructure and excitation at $x = 0$ for the highlighted case assuming dispersion (a) $\sigma_m = 0.15$, (b) $\sigma_m = 0.10$, (c) $\sigma_m = 0.05$ and (d) $\sigma_m = 0.01$. Red colours indicate low amplitude and blue colours indicate high amplitude levels.

Finally, Figure 11 presents the mean value and 5th and 95th percentiles of the amplitude of the transfer receptance and the real and imaginary parts of the metastructure, assuming $\sigma_m = 0.1$ and obtained with 1.000 Monte Carlo samples. It can be seen that the variability presented in the band gaps is mostly related to the variability in the imaginary part of the wavenumber, as expected. Moreover, the variability in the resonance peak between both attenuation bands in mostly due to the changed in the real part of the wavenumber. Also, the percentile upper and lower bounds are much smaller when compared to the previous case, presented Section 4.1. , which assumes $\sigma_m = 0.01$ and $\sigma_E = 0.03$.

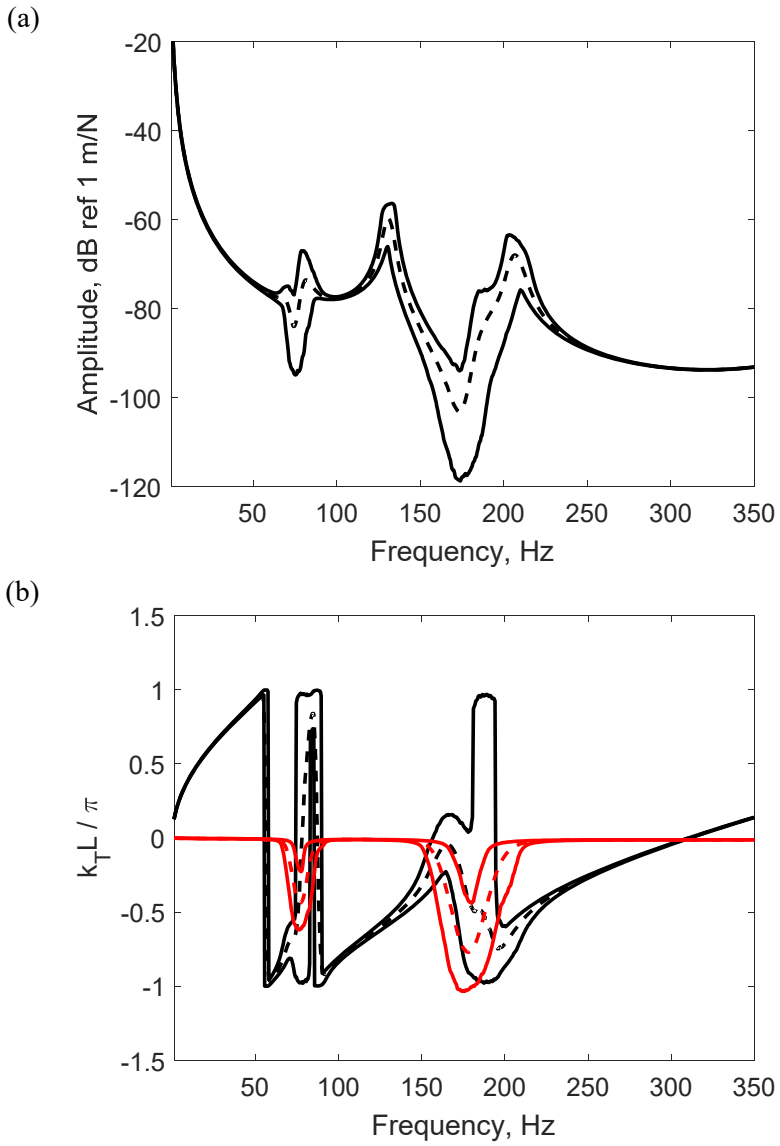

Figure 11: (a) The mean value (dashed line) and 5th and 95th percentiles (full line) of (a) the amplitude of the transfer receptance and (b) the real (black) and imaginary (red) parts of the metastructure for random samples considering only independent realizations of $\mathbf{m}_1$ and $\mathbf{m}_2$.

5. Concluding remarks

In this work, the effects of the manufacturing variability on the attenuation performance of a multi-frequency metastructure from additive manufacturing is investigated. The manufacturing tolerances of specimens produced from a Selective Laser Sintering process are assessed and variability levels are used to propose a stochastic model of the metastructure. It is shown that the geometrical parameters present negligible variability while the Young's modulus, total mass and consequently mass density have small variability. The experimental data has also shown a correlation between the Young's modulus and total mass of the test samples, which could have been induced by the underlying porosity of the material.

Moreover, an analytical model based on a transfer matrix approach is used to calculate transfer receptance due to a point time harmonic force of a metastructure designed with evenly spaced non-

symmetric resonators attached to a beam with Π-shaped cross-section in each unit cell. This configuration generated multifrequency attenuation due to each independent cantilever beam. Based on the experimental data from the test samples, a random field model is proposed for the tip masses of the resonators and the Young's modulus along the metastructure, using correlation models available in the literature for structures produced from additive manufacturing. The overall level of structural damping $n = 0.02$ played an important role on the both locally resonant and Bragg-scattering band gaps. The former was broadened while the latter, created due to the periodic plate inclusions, was annihilated.

Overall, it is shown that the mistuned resonators changed the vibration attenuation performance of the metastructure and that even small levels of variability, given by less than 1% for the mass and less than 3% for the Young's modulus can have a significant effect on the overall vibration attenuation performance of the metastructure when considered together. Smoother mass and Young's modulus spatial profiles, generated from sample of the proposed random field models, created band gaps with larger maximum attenuation in both band gaps while rougher spatial profiles presented a smaller maximum attenuation performance but a wider band gap. The same effect can be seen on the imaginary part of the equivalent normalized wavenumber of the finite length metastructure, that is used as a measure of the total attenuation change.

The case in which only the tip masses are considered to be random is also investigated. A similar behaviour to the previous case can be observed in terms of the smoother and rougher spatial profile changing band gap widening and maximum attenuation, however in this case each band gap is affected in an independent manner due to the independence on the tip masses values. Two statically identical profiles, i.e. same dispersion levels and correlation length, lead to qualitative changes on the band gaps created for each corresponding mass. Increasing values of dispersion eventually generated wave trapping in one of the band gaps while the had no such effect on the other.

Most importantly, it is shown that the investigation of the uncertainty due to manufacturing has to take into account the spatial correlation of the properties of the metastructure resonators.

Acknowledgments

The authors would like to acknowledge the support acquired by the H2020 DiaMoND project (Grant Agreement ID:785859), Royal Society Grant: PURSUIT, the Brazilian National Council of Research CNPq (Grant Agreement ID: 420304/2018-5) and the Federal District Research Foundation FAPDF (Grant Agreement ID: 0193.001507/2017).

References

[1] K. Bertoldi, V. Vitelli, J. Christensen, M. van Hecke, Flexible mechanical metamaterials, Nat. Rev. Mater. 2 (2017) 17066. doi:10.1038/natrevmats.2017.66.

[2] Y. Fan, M. Collet, M. Ichchou, L. Li, O. Bareille, Z. Dimitrijevic, A wave-based design of semi-active piezoelectric composites for broadband vibration control, Smart Mater. Struct. 25 (2016) 055032. doi:10.1088/0964-1726/25/5/055032.

[3] R. Hague, I. Campbell, P. Dickens, Implications on design of rapid manufacturing, Proc. Inst. Mech. Eng. Part C J. Mech. Eng. Sci. 217 (2003) 25–30. doi:10.1243/095440603762554587.

[4] R.D. Goodridge, C.J. Tuck, R.J.M. Hague, Laser sintering of polyamides and other polymers, Prog. Mater. Sci. 57 (2012) 229–267. doi:10.1016/j.pmatsci.2011.04.001.

[5] C. Sugino, Y. Xia, S. Leadenham, M. Ruzzene, A. Erturk, A general theory for bandgap estimation in locally resonant metastructures, J. Sound Vib. 406 (2017) 104–123. doi:10.1016/j.jsv.2017.06.004.

[6] D. Beli, A.T. Fabro, M. Ruzzene, J.R.F. Arruda, Wave attenuation and trapping in 3D printed cantilever-in-mass metamaterials with spatially correlated variability, Sci. Rep. 9 (2019) 5617. doi:10.1038/s41598-019-41999-0.
[7] P. Celli, B. Yousefzadeh, C. Daraio, S. Gonella, Bandgap widening by disorder in rainbow metamaterials, Appl. Phys. Lett. 114 (2019) 091903. doi:10.1063/1.5081916.
[8] L. Van Belle, C. Claeys, E. Deckers, W. Desmet, Measurement of dispersion curves for locally resonant metamaterials with damping, in: Proc. 27th Int. Conf. Noise Vib. Eng. ISMA 2016, 2016. https://lirias.kuleuven.be/handle/123456789/546033 (accessed April 20, 2017).
[9] C. Droz, O. Robin, M. Ichchou, N. Atalla, Improving sound transmission loss at ring frequency of a curved panel using tunable 3D-printed small-scale resonators, J. Acoust. Soc. Am. 145 (2019) EL72–EL78. doi:10.1121/1.5088036.
[10] J. Jung, H.-G. Kim, S. Goo, K.-J. Chang, S. Wang, Realisation of a locally resonant metamaterial on the automobile panel structure to reduce noise radiation, Mech. Syst. Signal Process. 122 (2019) 206–231. doi:10.1016/j.ymssp.2018.11.050.
[11] J.P. Den Hartog, Mechanical Vibrations, Dover Publications, 1985.
[12] P.F. Pai, Metamaterial-based Broadband Elastic Wave Absorber, J. Intell. Mater. Syst. Struct. 21 (2010) 517–528. doi:10.1177/1045389X09359436.
[13] Z. Liu, X. Zhang, Y. Mao, Y.Y. Zhu, Z. Yang, C.T. Chan, P. Sheng, Locally Resonant Sonic Materials, Science. 289 (2000) 1734–1736. doi:10.1126/science.289.5485.1734.
[14] M.J. Brennan, Some Recent Developments in Adaptive Tuned Vibration Absorbers/Neutralisers, Shock Vib. 13 (2006) 531–543. doi:10.1155/2006/563934.
[15] M. Ruzzene, A. Baz, Attenuation and localization of wave propagation in periodic rods using shape memory inserts, Smart Mater. Struct. 9 (2000) 805. doi:10.1088/0964-1726/9/6/310.
[16] M.-L. Wu, L.-Y. Wu, W.-P. Yang, L.-W. Chen, Elastic wave band gaps of one-dimensional phononic crystals with functionally graded materials, Smart Mater. Struct. 18 (2009) 115013. doi:10.1088/0964-1726/18/11/115013.
[17] C. Claeys, E. Deckers, B. Pluymers, W. Desmet, A lightweight vibro-acoustic metamaterial demonstrator: Numerical and experimental investigation, Mech. Syst. Signal Process. 70–71 (2016) 853–880. doi:10.1016/j.ymssp.2015.08.029.
[18] C. Claeys, N.G. Rocha de Melo Filho, L. Van Belle, E. Deckers, W. Desmet, Design and validation of metamaterials for multiple structural stop bands in waveguides, Extreme Mech. Lett. 12 (2017) 7–22. doi:10.1016/j.eml.2016.08.005.
[19] N.G.R. de Melo Filho, L. Van Belle, C. Claeys, E. Deckers, W. Desmet, Dynamic mass based sound transmission loss prediction of vibro-acoustic metamaterial double panels applied to the mass-air-mass resonance, J. Sound Vib. 442 (2019) 28–44. doi:10.1016/j.jsv.2018.10.047.
[20] G.L. Huang, C.T. Sun, Band Gaps in a Multiresonator Acoustic Metamaterial, J. Vib. Acoust. 132 (2010) 031003. doi:10.1115/1.4000784.
[21] Y.Y. Chen, M.V. Barnhart, J.K. Chen, G.K. Hu, C.T. Sun, G.L. Huang, Dissipative elastic metamaterials for broadband wave mitigation at subwavelength scale, Compos. Struct. 136 (2016) 358–371. doi:10.1016/j.compstruct.2015.09.048.
[22] E.J.P. Miranda, E.D. Nobrega, A.H.R. Ferreira, J.M.C. Dos Santos, Flexural wave band gaps in a multi-resonator elastic metamaterial plate using Kirchhoff-Love theory, Mech. Syst. Signal Process. 116 (2019) 480–504. doi:10.1016/j.ymssp.2018.06.059.
[23] P.F. Pai, H. Peng, S. Jiang, Acoustic metamaterial beams based on multi-frequency vibration absorbers, Int. J. Mech. Sci. 79 (2014) 195–205. doi:10.1016/j.ijmecsci.2013.12.013.
[24] E.J.P. Miranda Jr., J.M.C. Dos Santos, Flexural wave band gaps in multi-resonator elastic metamaterial Timoshenko beams, Wave Motion. 91 (2019) 102391. doi:10.1016/j.wavemoti.2019.102391.
[25] X. Xiao, Z.C. He, E. Li, A.G. Cheng, Design multi-stopband laminate acoustic metamaterials for structural-acoustic coupled system, Mech. Syst. Signal Process. 115 (2019) 418–433. doi:10.1016/j.ymssp.2018.06.004.
[26] J. Christensen, M. Kadic, O. Kraft, M. Wegener, Vibrant times for mechanical metamaterials, MRS Commun. 5 (2015) 453–462. doi:10.1557/mrc.2015.51.
[27] S.A. Cummer, J. Christensen, A. Alù, Controlling sound with acoustic metamaterials, Nat. Rev. Mater. 1 (2016) 16001. doi:10.1038/natrevmats.2016.1.

[28] Y. Zhang, F. Zhang, Z. Yan, Q. Ma, X. Li, Y. Huang, J.A. Rogers, Printing, folding and assembly methods for forming 3D mesostructures in advanced materials, Nat. Rev. Mater. 2 (2017) 17019. doi:10.1038/natrevmats.2017.19.
[29] Y. Wu, M. Yang, P. Sheng, Perspective: Acoustic metamaterials in transition, J. Appl. Phys. 123 (2017) 090901. doi:10.1063/1.5007682.
[30] A.T. Fabro, R. Sampaio, E.S. de Cursi, Wave attenuation in a metamaterial beam assembly with uncertainties, in: Proc. XVIII Int. Symp. Dyn. Probl. Mech. DINAME2019, Buzios, Brazil, 2019.
[31] F. Bloch, Über die Quantenmechanik der Elektronen in Kristallgittern, Z. Für Phys. 52 (1929) 555–600. doi:10.1007/BF01339455.
[32] H. Zhang, Y. Xiao, J. Wen, D. Yu, X. Wen, Flexural wave band gaps in metamaterial beams with membrane-type resonators: theory and experiment, J. Phys. Appl. Phys. 48 (2015) 435305. doi:10.1088/0022-3727/48/43/435305.
[33] A.T. Fabro, Neil.S. Ferguson, T. Jain, R. Halkyard, B.R. Mace, Wave propagation in one-dimensional waveguides with slowly varying random spatially correlated variability, J. Sound Vib. 343 (2015) 20–48. doi:10.1016/j.jsv.2015.01.013.
[34] Z. Hu, S. Mahadevan, Uncertainty quantification and management in additive manufacturing: current status, needs, and opportunities, Int. J. Adv. Manuf. Technol. 93 (2017) 2855–2874. doi:10.1007/s00170-017-0703-5.
[35] F. Lopez, P. Witherell, B. Lane, Identifying Uncertainty in Laser Powder Bed Fusion Additive Manufacturing Models, J. Mech. Des. 138 (2016) 114502-114502–4. doi:10.1115/1.4034103.
[36] E.A. Papon, A. Haque, S.B. Mulani, Process optimization and stochastic modeling of void contents and mechanical properties in additively manufactured composites, Compos. Part B Eng. (2019) 107325. doi:10.1016/j.compositesb.2019.107325.
[37] Z. Hu, S. Mahadevan, Uncertainty quantification in prediction of material properties during additive manufacturing, Scr. Mater. 135 (2017) 135–140. doi:10.1016/j.scriptamat.2016.10.014.
[38] Y. Huang, M.C. Leu, J. Mazumder, A. Donmez, Additive Manufacturing: Current State, Future Potential, Gaps and Needs, and Recommendations, J. Manuf. Sci. Eng. 137 (2015) 014001-014001–10. doi:10.1115/1.4028725.
[39] T. Moges, G. Ameta, P. Witherell, A Review of Model Inaccuracy and Parameter Uncertainty in Laser Powder Bed Fusion Models and Simulations, J. Manuf. Sci. Eng. 141 (2019) 040801-040801–14. doi:10.1115/1.4042789.
[40] Z. Wang, P. Liu, Y. Ji, S. Mahadevan, M.F. Horstemeyer, Z. Hu, L. Chen, L.-Q. Chen, Uncertainty Quantification in Metallic Additive Manufacturing Through Physics-Informed Data-Driven Modeling, JOM. 71 (2019) 2625–2634. doi:10.1007/s11837-019-03555-z.
[41] M.R. Machado, S. Adhikari, J.M.C. Dos Santos, J.R.F. Arruda, Estimation of beam material random field properties via sensitivity-based model updating using experimental frequency response functions, Mech. Syst. Signal Process. 102 (2018) 180–197. doi:10.1016/j.ymssp.2017.08.039.
[42] E. Vanmarcke, Random Field: Analysis and Synthesis, 2nd Revised and Expanded, Word Scientific, Cambridge, MA, 2010.
[43] R. Ghanem, P.D. Spanos, Stochastic Finite Elements: A Spectral Approach, Revised edition, Dover Publications, Minneola, N.Y., 2012.
[44] A. Der Kiureghian, J.-B. Ke, The stochastic finite element method in structural reliability, Probabilist Eng. Mech. 3 (1988) 83–91.
[45] R.Y. Rubinstein, D.P. Kroese, Simulation and the Monte Carlo method, Second Edition, John Wiley & Sons, Inc., Hoboken, NJ, USA, 2007.
[46] A. Tabaei, C.C. Mei, Viscous effects on Bragg scattering of water waves by an array of piles., Phys. Rev. E Stat. Nonlin. Soft Matter Phys. 79 (2009) 026314. doi:10.1103/PhysRevE.79.026314.
[47] L. Van Belle, C. Claeys, E. Deckers, W. Desmet, On the impact of damping on the dispersion curves of a locally resonant metamaterial: Modelling and experimental validation, J. Sound Vib. 409 (2017) 1–23. doi:10.1016/j.jsv.2017.07.045.
[48] B.R. Mace, Discussion of “Dynamics of Phononic Materials and Structures: Historical Origins, Recent Progress and Future Outlook” (Hussein, M. I., Leamy, M. J., and Ruzzene, M., 2014,

ASME Appl. Mech. Rev., 66(4), p. 040802), Appl. Mech. Rev. 66 (2014) 045502–045502. doi:10.1115/1.4027723.
[49] A.T. Fabro, N.S. Ferguson, B.R. Mace, Wave propagation in slowly varying waveguides using a finite element approach, J. Sound Vib. 442 (2019) 308–329. doi:10.1016/j.jsv.2018.11.004.
[50] John Heading, An Introduction to Phase-Integral Methods, Reprinted edition, Dover Publications, New York, USA, 2013.
[51] J. Zhu, Y. Chen, X. Zhu, F.J. Garcia-Vidal, X. Yin, W. Zhang, X. Zhang, Acoustic rainbow trapping, Sci. Rep. 3 (2013) 1728. doi:10.1038/srep01728.
[52] Z. Tian, L. Yu, Rainbow trapping of ultrasonic guided waves in chirped phononic crystal plates, Sci. Rep. 7 (2017) 40004. doi:10.1038/srep40004.